8586–8598 *Nucleic Acids Research, 2011, Vol. 39, No. 19* *Published online 10 July 2011*
doi:10.1093/nar/gkr565

Molecular sensing by the aptamer domain of the FMN riboswitch: a general model for ligand binding by conformational selection

Quentin Vicens, Estefanía Mondragón and Robert T. Batey*

Department of Chemistry and Biochemistry, University of Colorado, Boulder, CO 80309-0215, USA

Received May 9, 2011; Revised June 20, 2011; Accepted June 21, 2011

ABSTRACT

Understanding the nature of the free state of riboswitch aptamers is important for illuminating common themes in gene regulation by riboswitches. Prior evidence indicated the flavin mononucleotide (FMN)-binding riboswitch aptamer adopted a 'bound-like' structure in absence of FMN, suggesting only local conformational changes upon ligand binding. In the scope of pinpointing the general nature of such changes at the nucleotide level, we performed SHAPE mapping experiments using the aptamer domain of two phylogenetic variants, both in absence and in presence of FMN. We also solved the crystal structures of one of these domains both free (3.3 Å resolution) and bound to FMN (2.95 Å resolution). Our comparative study reveals that structural rearrangements occurring upon binding are restricted to a few of the joining regions that form the binding pocket in both RNAs. This type of binding event with minimal structural perturbations is reminiscent of binding events by conformational selection encountered in other riboswitches and various RNAs.

INTRODUCTION

Since the discovery that certain mRNAs can directly bind metabolites to regulate their own expression [reviewed in (1,2)], questions pertaining to the mechanistic details of these 'riboswitches' have abounded. In particular, upon metabolite binding to the ligand-binding (*aptamer*) domain, the downstream 'expression platform' is partitioned to one of two mutually exclusive secondary structures by the 'switching sequence', a stretch of nucleotides shared between these two domains (3,4). However, such a switch, particularly within transcriptional regulators, may not be reversible, so that once RNA polymerase has escaped the rho-independent transcriptional terminator; the riboswitch can no longer abort transcription (5,6). Thus, these RNA sensors only have a short temporal window in which to exert their regulatory effect. The aptamer must be able to fold efficiently, rapidly bind a metabolite and transmit its status to the actively transcribing downstream expression platform. The nature of the communication between these two domains has been only partly addressed.

To help understand how ligand binding determines which of the two mutually exclusive riboswitch structures will be adopted, the 3D structures of over 10 aptamer domains bound to corresponding metabolites have been solved [e.g. (7–9) and all reviewed in (10,11)]. In each of these, the ligand is adjacent to, or directly interacts with nucleotides of the switching sequence (3,7). The resulting stabilization of this particular conformation of the aptamer domain makes the switching sequence unavailable to participate in formation of an alternative secondary structure (2,3).

Similar levels of detail about the free states of these RNAs have been scarce. But in each of the four crystal structures of free aptamers solved to date (12–16), the RNA architecture closely resembles that of the ligand bound state. Furthermore, evidence from biochemical techniques suggests that these 'bound-like' structures trapped by the crystal lattice might represent the active conformation capable of productively binding ligand (13). Recently, small angle X-ray scattering (SAXS) data provided further support to such ligand-binding mechanism, by showing that the flavin mononucleotide (FMN) riboswitch aptamer from *Bacillus subtilis* (Figure 1) is globally folded at physiological magnesium concentration and undergoes little, if any, conformational change upon FMN binding (17). In-line and nuclease probing

*To whom correspondence should be addressed. Tel: +303 735 2159; Fax: +303 735 1347; Email: robert.batey@colorado.edu
Present addresses:
Quentin Vicens, Department of Molecular Biology, Aarhus University, 8000 Aarhus C, Denmark.
Estefanía Mondragón, Mayo Clinic, Rochester, MN 55905, USA.

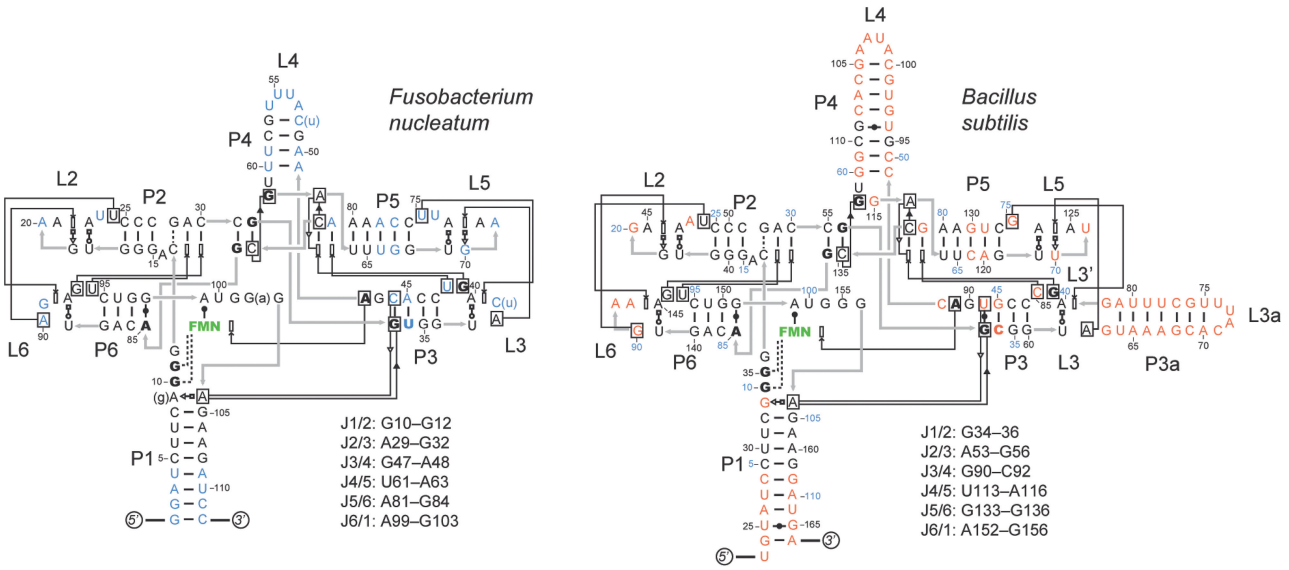

Figure 1. Secondary structure diagrams of the FMN riboswitches from *F. nucleatum* (left) and *B. subtilis* (right) used in this study. Black letters, nucleotides conserved between the two species; blue letters, nucleotides found only in *F. nucleatum*; orange letters, nucleotides found only in *B. subtilis*; green letters, FMN; bold letters, nucleotides interacting with FMN, either directly or via a magnesium ion (19); lower case letters in parentheses, nucleotide changes in the variant used by (19); black figures, species-specific numbering; blue figures, *F. nucleatum* numbering overlayed on the *B. subtilis* sequence. Inset at the bottom right of each diagram, nucleotide ranges of each joining region. Interactions labeled using the Leontis–Westhof nomenclature (67).

of the aptamer domains from *B. subtilis*, but also from *Fusobacterium nucleatum* (Figure 1), implicated a number of nucleotides that could be involved in ligand-dependent conformational changes (18,19). Overall, the picture of genetic regulation emerging from these studies is that of RNAs that have the ability to act as regulatory switches without needing to undergo large ligand-induced conformational changes (13,20,21).

Here, we present a nucleotide-level analysis of FMN riboswitch aptamers from *B. subtilis* and *F. nucleatum* (Figure 1). We monitored the structure and folding of the *B. subtilis* and *F. nucleatum* aptamers in solution using the selective 2′-hydroxyl acylation analyzed by primer extension (SHAPE) chemical footprinting technique (22). Additionally, we solved the structures of both the free and bound forms of a sequence variant of the *F. nucleatum* aptamer that had been used in prior crystallographic studies (see 'Materials and Methods' section) (19). Our results yield specific insights into local conformational changes in the FMN aptamer domain associated with folding and ligand binding. These changes are mostly similar for the two RNAs tested, which makes for an important consideration to drug designers (23,24), considering the broad distribution of FMN riboswitches in the bacterial kingdom (25,26). We also demonstrate that the aptamer domain of the FMN riboswitch folds cooperatively in presence of magnesium, irrespective of the presence of a ligand. Finally, we show that the only regions undergoing conformational changes upon ligand binding are a subset of joining regions that immediately contact FMN in the crystal structure, including nucleotides from the switching sequence within J1/2. Our comparison between the free and bound forms suggests that J1/2 and J6/1 serve as the gate to a binding pocket that is maintained in an 'open' state by J3/4 and J4/5. From this work, and from the other structures of an aptamer domain in absence of ligand (12–16) as well as from various findings on the behavior of aptamer domains in solution (12,13,27–29), a model emerges for ligand binding to riboswitches by conformational selection.

MATERIALS AND METHODS

RNA preparation for chemical probing experiments

The *B. subtilis* RNA variant was designed to contain residues 23–166 of the *165 ribD RFN* element from *Bacillus subtilis* used in previous *in vitro* studies (Rfam accession #X59538.1, position range 81–225) (17,18). The *F. nucleatum* RNA variant was designed to contain residues 1–112 from a natural variant of the *RFN* element from *F. nucleatum subsp. nucleatum ATCC 25586* (Rfam accession #AE009951.2) that was recently analyzed by crystallography (19). The sequence is found at positions 10 346–10 461 and contains five purine-to-purine and pyrimidine-to-pyrimidine substitutions from the sequence found at positions 2491–2606 (Figure 1). These RNAs represent the earliest stage in the transcriptional timeline in which the aptamer has been transcribed and magnesium-dependent tertiary structure has been acquired (3,30). Immediately following this sequence in the *B. subtilis* FMN riboswitch, a programmed transcriptional pause gives the aptamer a multisecond period to interrogate the cellular environment in the absence of the influence of downstream sequences that compete to form alternative structures (6). Both riboswitch aptamers were inserted into a structure cassette for SHAPE mapping (31). DNA template synthesis, transcription reactions and RNA purification were

performed as previously described (32), with minor modifications (Methods in Supplementary Data).

SHAPE Mg titrations

Four independent mapping experiments were performed according to published SHAPE protocols (31). The RNA was diluted to a concentration of 2.0 μM in 50 mM HEPES pH 8.0, incubated for 2 min at 95°C followed by 3 min at 4°C. Two parts of this RNA solution were combined to one part of a folding buffer so that the following buffer and ionic concentrations would be reached: 100 mM KCl, 0–15 mM $MgCl_2$ ([$MgCl_2$] chosen: 0, 0.025, 0.1, 0.25, 0.5, 1.0, 2.0, 5.0, 15.0 mM (replicates 1–3); 20 and 50 mM $MgCl_2$ were added for replicate 4), 50 mM HEPES pH 8.0, ±10.0 μM FMN (Sigma-Aldrich). This mixture was incubated for 10 min at 37°C.

NMIA or 1M7 modification (33) was performed in the presence of 6.5 mM NMIA or 1M7 (gift from S. Mortimer and K. Weeks) for 45 min (NMIA), 30 min (1M7, no FMN; *B. subtilis* RNA), or for 12 min (1M7, with FMN; *B. subtilis* RNA) at 37°C, at each magnesium concentration specified above. Samples were precipitated for 16 h at −20°C in 70% EtOH, 100 mM Na acetate pH 5.3, in the presence of 20 μg of glycogen, centrifuged for 35 min at 13 500*g*, dried for 10 min under vacuum and resuspended in 9.0 μl 0.5× T.E. buffer (10 mM Tris, 1 mM EDTA, pH 8.0).

Primer extension by reverse transcription was performed as described (31), except that the extension step was performed for 15 min at 50°C. Primers used for the extension were designed to pair either with a binding site in the 3′ structure cassette (for *B. subtilis* and *F. nucleatum*) or with an internal site (for *B. subtilis*), in order to monitor the 5′-end of the RNA. The internal primer was complementary to nucleotides 105–142 (3′-read), or 82–112 (5′-read). Extensions products were resolved by analytical gel electrophoresis, as described (32) (Methods in Supplementary Data).

The gel image (*.gel* file; Supplementary Figure S1) was opened and processed in SAFA v. 1.1 (34,35). For normalization purposes, a set of 4 nt was determined that comprised the nucleotides most commonly selected by SAFA throughout the four independent experiments (Methods in Supplementary Data, Supplementary Figures S1 and S2). The option of applying factors to correct for linear correlation between NMIA reactivity and magnesium concentration observed for a model nucleotide was initially considered, as suggested in (33). However, we did not carry out this correction after observing no significant change in NMIA reactivity as a function of magnesium concentration with the *B. subtilis* RNA (Supplementary Figure S2).

The resulting normalized *.txt* file was further analyzed by calculating the extent of adduct formation (E) and the fraction folded (F) for each residue at each magnesium concentration tested (36). The extent of adduct formation of residue i for $MgCl_2$ concentration x is described by:

$$E_{ix} = \frac{I_{ix} \times (\sum_{I_{iL}})}{\sum_{I_{ix}} - I_{iL}} \quad (1)$$

where I_{ix} is the number of counts for residue i, ΣI_{ix} is the sum of the counts for all assessed positions when $[MgCl_2] = x$, and I_{iL} is the lowest number of counts for residue i observed at any [$MgCl_2$] (typically <1.0 mM). The fraction folded is expressed as $F_{ix} = E_{ix}/E_{iH}$, where E_{iH} is the highest extent of adduct formation at position i calculated at any [$MgCl_2$] (typically >1.0 mM). F_{ix} provides an estimate of the relative extent of folding at each residue, assuming a two-state model.

The fraction folded was plotted against the magnesium concentration on a semi-log graph (36). The sigmoidal curve—observed for cooperative transitions—was fitted using a Hill equation in Kaleidagraph v. 4.0 (Synergy Software). Obvious outliers were ignored for the fitting procedure, according to the following criteria: similarity of the fits between independent experiments and similarity of the fits between adjacent residues, unless a change or discrepancy was revealed on the gel. Mid-point values for K_D (e.g. $[Mg]_{1/2}$) and n_H (cooperativity index) were extrapolated from the fit when the correlation coefficient R^2 was >0.91 (Supplementary Figure S3). These values were averaged and the standard error of the mean was calculated from a statistical propagation of error analysis.

SHAPE temperature surveys

Three independent mapping experiments were performed as described above, but only at 5.0 mM $MgCl_2$. Temperatures were sampled in 5°C intervals over a 20–90°C range. NMIA modification at each temperature proceeded for five half-lives as described (37). Samples were precipitated and extended by reverse transcription as described above, except that the internal primer for the *B. subtilis* riboswitch was not employed. Products were similarly analyzed by gel electrophoresis.

The gel image (*.gel* file; Supplementary Figure S4) was opened in SAFA v. 1.1 (34,35) and processed as described above. Because of hyper-modification of the RNA at temperatures >65°C (Supplementary Figure S4), invariant residues were chosen for normalization that matched some or all of the following criteria: (i) they corresponded to RT stops (identified for example from temperature survey experiments performed in absence of NMIA; Supplementary Figure S5); (ii) their intensity decreased as temperature increased, and possibly increased again when $T > 75$°C (e.g. see nucleotides 123 and 142, Supplementary Figure S5); (iii) they spanned the gel (less critical for the long runs; Supplementary Figures S4 and S5); (iv) they gave consistent results when applied to independent experiments (Supplementary Figure S6). We settled on the set of invariants that would lead to normalized reactivities on average better fitted to a curve describing a unimolecular melting transition (Supplementary Figures S4–S7 and Methods in Supplementary Data) (37). Fitting ignored data points that were obvious outliers (similar criteria as for the fits of the Mg titrations) or that showed a significant decrease in reactivity at higher temperatures (32).

Mid-point values for T_m (melting temperature) were extrapolated from the fit when the correlation coefficient R^2 was >0.91 (Supplementary Figure S6). These values

were averaged and the standard error of the mean was calculated from a statistical propagation of error analysis.

Crystallization

In our crystallization trials, we employed the two-piece *F. nucleatum* FMN riboswitch used in the study by Serganov *et al*. (19). Strand 'B' was engineered to include an optimal transcription start site [alteration of 5′-GCU-3′ in (19) to 5′-GGA-3′; strand 'A' was correspondingly engineered to maintain Watson–Crick pairing in P4; Supplementary Figure S8]. The 2-nt overhang at the 3′ end of strand 'A' (19) was kept, but changed from 5′-UU-3′ into 5′-AU-3′. This 'wild-type' sequence of the FMN riboswitch (Supplementary Figure S8) was used as the starting point of a mutational survey, according to a strategy similar to that employed for the SAM-I riboswitch (38) (Supplementary Table S5). Following synthesis of each strand by transcription using T7 RNA polymerase, the strands were purified using standard techniques (32,39), and annealed using the published protocol (19). The set of RNAs that yielded the highest quality diffraction in both the free and FMN-bound forms were: (strand 'A') 5′-GGAUCUUCGGGGCAGGGUGAAAUUCCCGACCGGUGGUAUAGUCCACGAAUCCAU and (strand 'B') 5′-GGAUUGAUUUGGUGAAAUUCCAAAACCGACAGUAGAGUCUGG-AUGAGAGAAGAUUCG (same sequence as our 'wild-type' but with a 3′-G overhang on strand 'B'; Supplementary Figure S8 and Supplementary Table S5). After annealing, the two-piece RNA was crystallized using the hanging drop method in which 1 µl of 100 µM RNA was mixed with 1 µl of mother liquor and incubated at 20°C. The mother liquor contained the following components: 11% PEG-4000, 0.32 M $MgCl_2$ and 0.01 M Tris–Cl, pH 8.4 (free RNA); 15% PEG-monomethyl 550 ether, 0.1 M $MgCl_2$, and 0.05 M Na–HEPES, pH 7.0 and 1 mM FMN (FMN-bound RNA). The crystals took 2–3 days to reach full size (~150 µm in each dimension). Prior to cryoprotection, the crystals were dehydrated in a first step over mother liquor plus 10% mother liquor and incubated at 20°C for 12–16 h. The crystals were cryoprotected by soaking for ~5 min in mother liquor plus 25% glycerol and flash frozen in liquid nitrogen.

Data collection and refinement

Data for crystals of the free and bound states were collected on beamline X29A (free) and X25A (FMN bound) at the Brookhaven National Synchrotron Light Source. The resulting data sets were integrated and scaled using the *HKL2000* package (40). As an initial search model for molecular replacement, the previously determined structure of the FMN riboswitch aptamer domain (PDB ID 3F2Q) (19) was used, after removal of solvent, metal ions, and FMN. Following calculation of an initial electron density map, the model was manually adjusted in *COOT* v. 0.6 (41), along with addition of ligand, where appropriate. The model was further refined using simulated annealing in *CNS* v. 1.1 (42) and semi-automated building of solvent and hydrated metal ions. The final stages of refinement were performed using *PHENIX* v. 1.7-650 (43). Refinement comprised four macro cycles of energy minimization of individual coordinates, and refinement of group atomic displacement parameters including translation/libration/screw (TLS) vibrational motions for 12 segments, of occupancy, and of ordered solvent (water) (44). Models were validated using *MOLPROBITY* (45) and adjusted for lowest all-atom clash scores by further refinement using a reference A-form helix built in *COOT* (5′-CCACUUCCACAUC-3′ and complementary strand), with automatic optimization of the X-ray target weight. Final R/R_{free} (%) were 20.6/25.7 (free) and 20.4/23.1 (bound) (Table 2). 3D structures were superimposed using *THESEUS* (46). Figures were prepared using the *MacPyMOL* Molecular Graphics System, v. 0.99 (Schrödinger, LLC). Models and structure factors were deposited in the RCSB Protein Data Bank under the PDB IDs 2YIF (free) and 2YIE (FMN bound).

RESULTS

The aptamer domain of the FMN riboswitch is globally pre-organized in absence of ligand

To explore how the local and global architectures of the FMN aptamer were affected by FMN, we carried out SHAPE structure mapping, which involves the reaction between *N*-methylisatoic anhydride (NMIA) and the 2′-hydroxyl group of nucleotides not embedded in Watson–Crick pairs (22). In the case of riboswitches, the differences between reactivities to NMIA in absence and in presence of the cognate ligand reflect differences in the degrees of tertiary architecture adopted by the two populations of structures being analyzed (13,32). Furthermore, we observed reactivity changes both over a range of magnesium concentrations (0–15 mM) at a constant temperature (37°C), as well as over a range of temperatures (20–90°C) at a constant magnesium concentration (5.0 mM). These complementary strategies allow for a nucleotide-level monitoring of folding cooperativity and of changes in conformational sampling associated with diverse degrees of tertiary structure formation within the RNA population (13,32,37).

Visual inspection of the magnesium titration data revealed that in both the *B. subtilis* and *F. nucleatum* RNAs, most of the nucleotides known to participate in secondary structure elements (Figure 1) were unmodified by NMIA in absence of magnesium, regardless of the presence of FMN (Figure 2a and b). Upon increase of the magnesium concentration to 0.25–1 mM, the remaining nucleotides in helical regions (parts of paired regions P4 and P5 for *F. nucleatum*) underwent transitions from higher to lower NMIA modification levels. The exception was loops L3a and L4, which underwent a converse transition (Figure 2a and b). This behavior highlighted the formation of the structural features seen in the crystal structure of the *F. nucleatum* RNA (19), such as the formation of tertiary interactions between peripheral domains like T-loop/T-loop receptor interactions (L2–L6 and L3–L5) and loop–helix interactions (L6–P2 and L3–P5). It also denoted a particular structural transition leading to the stabilization of P3a and P4 and the

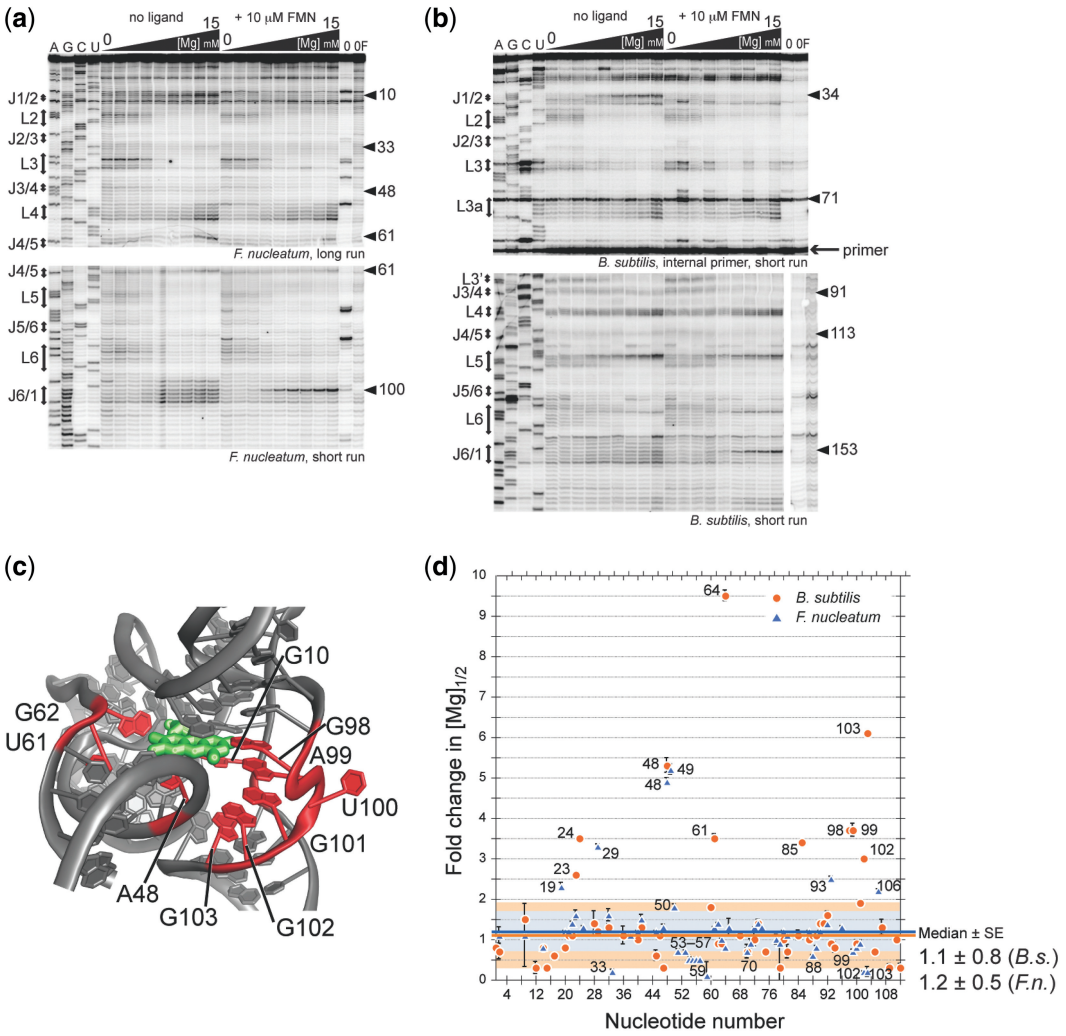

Figure 2. Magnesium-dependent chemical probing of the *F. nucleatum* and *B. subtilis* RNAs. (**a**) Long run (top) and short run (bottom), obtained with the *F. nucleatum* riboswitch. (**b**) Short run after extension using an internal primer (top) and short run after extension using the regular primer (bottom), obtained with the *B. subtilis* riboswitch. [$MgCl_2$] were 0, 0.025, 0.1, 0.25, 0.5, 1.0, 2.0, 5.0 and 15.0 mM. Controls: Lane 0, no Mg, no ligand, no NMIA; lane 0 F, no Mg, 10 mM FMN, no NMIA. Arrowheads: residues of interest (see main text). The gels were aligned in SAFA (34,35). Full-length gels and additional control experiments shown in Supplementary Figures S1 and S2. (**c**) The nucleotides that undergo FMN-induced conformational changes in *F. nucleatum* and *B. subtilis* are shown in red on the crystal structure of the FMN-bound riboswitch (19). (**d**) Fold change in $[Mg]_{1/2}$ upon ligand binding (+ligand/no ligand) for both riboswitches. Colored solid line (blue, *F. nucleatum*; orange, *B. subtilis*), median value. Shaded box (same color coding), standard error around the median. In panel (d), the numbering of the *B. subtilis* RNA was aligned to that of the *F. nucleatum* RNA, as shown in Figure 1.

progressive exposure to the solvent of L3a and L4. Together, these findings supported that both aptamer domains were globally folded at physiological magnesium concentrations (0.5–1.5 mM). This observation is in agreement with previous studies performed on these two aptamer domains by either in-line probing (18,24), enzymatic footprinting (19) or small angle X-ray scattering (SAXS) (17).

FMN marginally increases RNA folding cooperativity and stability

The degree of cooperativity of the folding transitions observed in the magnesium titrations was quantified as described previously for Fe(II)–EDTA chemical probing data acquired for the *Tetrahymena* group I intron (36). Using a mathematical model that assumes two-state folding transitions, we calculated the fraction of molecules in the final folded state, at each position of the RNA and at each magnesium concentration tested (see 'Materials and Methods' section). The resulting sigmoidal curves with sharp transitions indicated a high cooperativity of folding for ~65% of the residues that displayed reactivity change to NMIA as a function of magnesium concentration (not all residues displayed a cooperative folding behavior both in absence and in presence of ligand; Supplementary Figures S1–S3, Supplementary Tables S1 and S2). The average of the corresponding midpoint ($[Mg^{2+}]_{1/2}$) values was within 0.7–1.0 mM for both RNAs in the absence of FMN, and slightly lower in presence of ligand (Table 1). Furthermore, the highest $[Mg^{2+}]_{1/2}$ value was lower in presence of FMN for the *B. subtilis* RNA (Table 1). Finally, out of all the

Table 1. Transition midpoints for magnesium titrations

	No ligand		10 μM FMN	
	Fusobacterium nucleatum	*Bacillus subtilis*	*Fusobacterium nucleatum*	*Bacillus subtilis*
Average	0.9 ± 0.2[a]	1.0 ± 0.2	0.7 ± 0.1	0.8 ± 0.1
Lowest	0.1 ± 0.02	0.1 ± 0.02	0.1 ± 0.02	0.1 ± 0.01
Highest	5.4 ± 2.5	8.6 ± 4.1	4.2 ± 2.4	4.5 ± 2.8

[a]$[Mg^{2+}]_{1/2}$ values ± standard error of the mean (mM).

nucleotides that possessed a mid-point value, 16% (*F. nucleatum*) and 22% (*B. subtilis*) had a $[Mg^{2+}]_{1/2}$ value superior to 1.5 mM in absence of ligand, compared to only 8% in presence of FMN (Supplementary Tables S1 and S2). These results supported a slight, but reproducible, stabilization of the aptamer domain upon FMN binding through a small increase in folding cooperativity.

The SHAPE temperature surveys further support a similar but somewhat enhanced folding of the FMN riboswitch aptamer domain in presence of FMN. Examination of the gels revealed that both aptamers unfolded similarly as temperature increased, as visualized by the progressive augmentation in the number of bands, particularly around 65°C (Figure 3a and b). The average observed melting point (T_m) calculated from the two-state folding transition of each measurable nucleotide (see 'Materials and Methods' section) slightly increased upon ligand binding [average T_m ± standard deviation (SD)]: 64.9 ± 4.6°C (unbound) and 69.3 ± 4.3°C (FMN bound) for *B. subtilis*; 60.5 ± 8.2°C (unbound) and 67.7 ± 5.6°C (FMN bound) for *F. nucleatum* (Supplementary Tables S3 and S4). Overall, the low levels of stabilization of the global structure and of folding enhancement we observed upon FMN binding are consistent with a mostly preformed architecture in absence of ligand. Furthermore, productive interaction of the FMN with the core of the junction provides only a modest additional stabilization of the RNA.

The major conformational changes associated with FMN binding are restricted to the joining regions that define the ligand-binding site

In spite of this general pre-organized state of the aptamer domain, striking changes in banding patterns were noted upon addition of FMN within joining regions J1/2 (residues 10 in *F. nucleatum*, and 34 in *B. subtilis*), J3/4 (residues 48 in *F. nucleatum*, and 91–92 in *B. subtilis*), J4/5 (residues 61–62 in *F. nucleatum*, and 113–114 in *B. subtilis*) and J6/1 (residues 98–103 in *F. nucleatum*, and 151–156 in *B. subtilis*) (Figure 2a and b). In absence of ligand, these residues displayed an increasing reactivity to NMIA upon magnesium concentration increase. In presence of FMN, all of these residues except one (U100 in *F. nucleatum*, and its equivalent U153 in *B. subtilis*) showed a decreased reactivity at all magnesium concentrations tested. This result is consistent with the structural organization of the FMN-binding site around FMN as seen in the crystal structure of the *F. nucleatum* FMN-bound aptamer domain (19). Nucleotides in J1/2, J3/4, J4/5 and A98 and A99 in J6/1 are located within 4 Å of FMN (Figure 2c) and most interact directly with FMN via hydrogen bonds and π-stacking. As suggested by its strong modification by NMIA in presence of FMN, U100 is bulged out, facing the solvent, in a flexible and highly reactive conformation (37,47) (Figure 2a–c). The remaining residues in J6/1 that displayed decreased reactivity to NMIA (98, 101–103) are not part of the first layer of residues that directly contact FMN, but are constrained through interactions with residues that contact FMN. In summary, the drop in reactivity to NMIA upon addition of the ligand observed for these joining region nucleotides inferred that ligand-induced stabilization happens principally at the binding site but extends to J6/1 nucleotides located up to 10 Å away.

In order to assess whether the different conformations of these joining regions in the free and FMN-bound populations were accompanied by changes in their dependence on the magnesium concentration for folding, we plotted the fold change in $[Mg^{2+}]_{1/2}$ values for each residue (Figure 2d). While >90% of the residues showed no significant fold change, fold change in $[Mg^{2+}]_{1/2}$ values were observed principally for nucleotides within J3/4, J4/5 and J6/1, as well as nucleotides adjacent to the joining regions (33 adjacent to J2/3, 49 and 50 adjacent to J3/4, 64 adjacent to J4/5, 85 adjacent to J5/6, and 98 adjacent to J6/1; aligned numbering for *B. subtilis* and *F. nucleatum*, Figure 1). These changes were predominantly comprised between 4 and 9 and observed in the *B. subtilis* aptamer domain mostly (Figure 2d), which indicated that for this RNA, a larger magnesium concentration was required to achieve the local reorganization of the binding pocket conducive to FMN binding. This somewhat unexpected observation could be linked to elongated P3 and P4 whose presence could affect the reorganization at J3/4 and J4/5 observed between the free and bound structures (see below).

Finally, we calculated the T_m differences between the free and the FMN-bound populations (ΔT_m, = $T_{m,bound} - T_{m,free}$) to specifically highlight the effect of FMN on folding of the joining regions (Supplementary Tables S3 and S4). Although the average ΔT_m was typically comprised within 0–5°C for most of the RNA (see above), the highest ΔT_m values were ~20–40°C for J1/2 and J6/1 of *F. nucleatum*, and about ~10–30°C for *B. subtilis* (Figure 3c and d). Moderate ΔT_m values were also observed at J3/4 and J4/5 (~4–8°C for *F. nucleatum*; ~9–16°C for *B. subtilis*). Together with the results of the magnesium survey, these findings indicated a ligand-induced conformational stabilization of the joining regions around the binding pocket. When these findings were combined to the observation of higher observed T_m values (by ~10°C) for residues belonging to P1 in the bound form (Figure 3c and d; Supplementary Tables S3 and S4), they also offered evidence for stabilization of the switching sequence upon ligand binding (residues 6–11 in *F. nucleatum* numbering). Such effect could promote formation of the transcription terminator in presence of FMN (18).

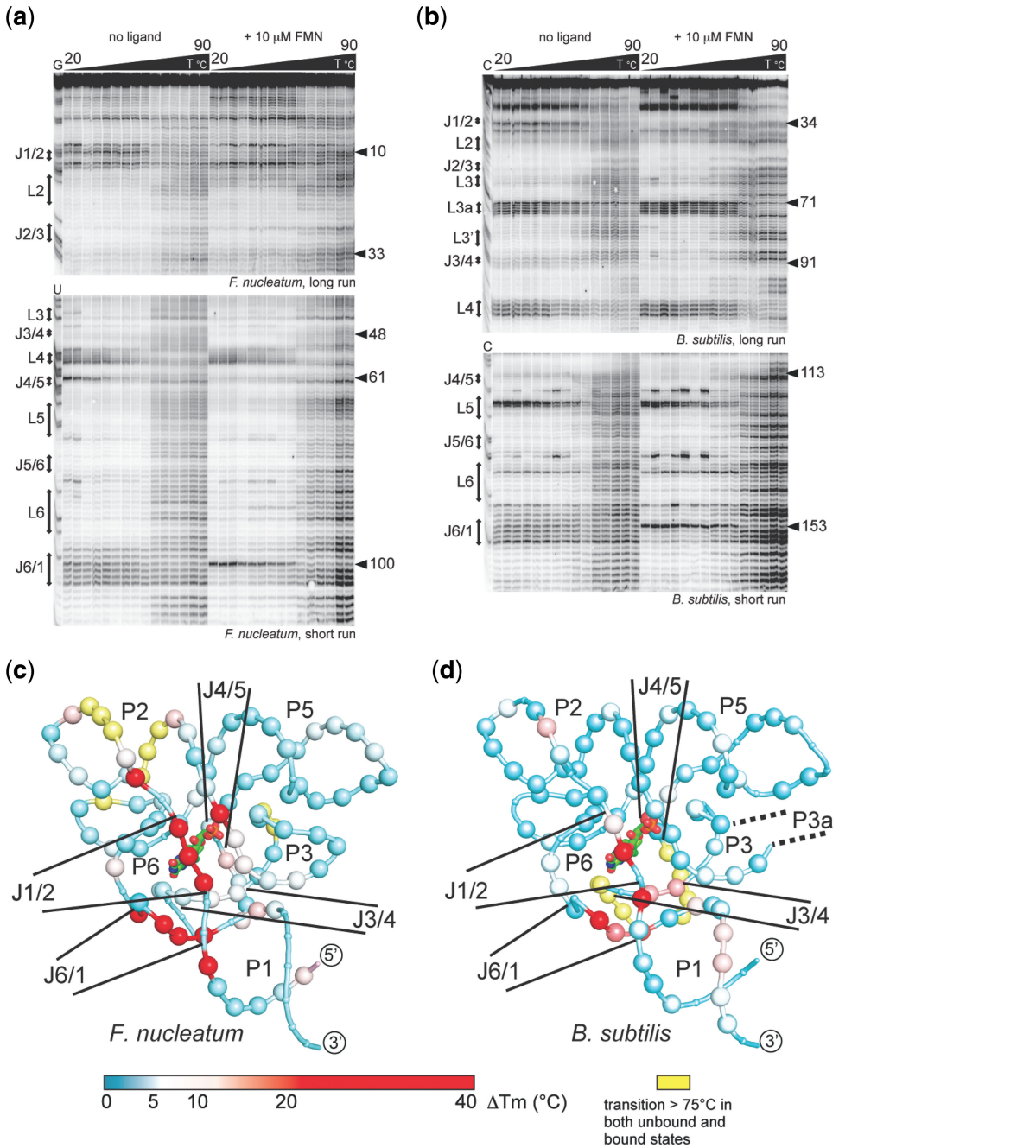

Figure 3. Temperature-dependent chemical probing of the *F. nucleatum* and *B. subtilis* RNAs. (**a**) Long run (top) and short run (bottom), obtained with the *F. nucleatum* riboswitch. (**b**) Long run (top) and short run (bottom), obtained with the *B. subtilis* riboswitch [aligned in SAFA (34,35)]. Temperature was varied by 5°C increments in a 20–90°C range. Arrowheads: residues of interest (see main text). Full-length gels and additional control experiments shown in Supplementary Figure S3. (**c**) Representation of the average ΔT_m per residue obtained for the *F. nucleatum* RNA superimposed on the *F. nucleatum* structure (PDB ID: 3F2Q; (19); nucleotide alignment as in Figure 1). Each phosphate group is shown as a large sphere (available ΔT_m value) or a small sphere (undetermined ΔT_m value). Color according to the magnitude of the Tm difference (see scale bar). FMN shown as sticks, and colored per atom type, with green for carbon atoms. (**d**) Same as (c), but with the values obtained for the *B. subtilis* RNA superimposed on the *F. nucleatum* structure. The location of the P3a extension present in *B. subtilis* but not *F. nucleatum* is indicated by dashed lines.

FMN binding induces unstacking at J3/4 and a conformational shift at J4/5

The similarity of the aptamer domain global structure in absence and in presence of ligand as characterized by SHAPE and by previous studies (17–19,24) prompted us to crystallize the aptamer domain of *F. nucleatum* in absence of ligand. This strategy had been previously successful for the lysine and the SAM-I riboswitches, for which it helped delineate ligand-induced conformational changes (13,16). First, we sought to optimize the

crystallization in presence of FMN of a two-piece construct reported in the original publication (*Fnu*O) (19). We surveyed a total of 36 mutations at 18 positions in the RNA, which resulted in a total of 378 combinations of the two strands (Supplementary Figure S8 and Supplementary Table S5). Crystallization and diffraction quality were the most affected by mutations of U100 and the addition of a 3′ overhang on strand 'B'. The best variant (*Fnu*M) had the same sequence as that of the original report (19), except for base pair swaps within P4 to optimize transcription, a 5′-AU-3′ instead of a 5′-UU-3′ overhang at the 3′-end of strand 'A', and a G overhang at the 3′-end of strand 'B'. While these changes significantly shortened crystallization time (from 1–4 weeks to 24 h), they did not yield any improvement in resolution (Table 2). At 2.95 Å resolution, the 3D structures of *Fnu*M and *Fnu*O bound to FMN were identical (maximum likelihood rmsd = 0.06 Å), which warranted the use of the faster crystallizing *Fnu*M for crystallization trials in absence of ligand.

Crystals of *Fnu*M in absence of ligand also grew in ~24 h, but diffracted to lower resolution (3.3 Å; Table 2). The RNA was also more disordered, as indicated by the higher average atomic displacement parameter than for the structure of the bound form (Table 2). Similar trends of lower resolution and higher disorder were previously observed for free forms of riboswitches (13,16). However, similar crystallization conditions, identical space group and similar cell parameters suggested that the global structure of the RNA was retained, thus leading to crystal formation through similar packing interactions. Furthermore, we noticed that the structure of *Fnu*M bound to FMN could be obtained as well by adding FMN to the cryoprotecting solution prior to data collection (data not shown). Hence, the crystallized free RNA was capable of productively binding FMN, indicating it was in an active state.

Table 2. Data collection and structure refinement statistics

	Free	FMN bound
Data collection		
Space group	$P3_121$	$P3_121$
Cell dimensions $a = b$, c (Å); $\alpha = \beta$, γ°.	73.5, 135.2; 90, 120	73.7, 139.3; 90, 120
Wavelength (Å)	0.9795	0.9795
Resolution range (Å)	40–3.3 (3.42–3.30)[a]	40–2.95 (3.06–2.95)
No. of observed reflections	38 995	83 959
No. of unique reflections	6627 (593)	17 834 (1773)
Redundancy	5.9 (4.0)	4.7 (4.7)
Completeness (%)	98.1 (90.1)	99.3 (100)
$<I/\sigma(I)>$	22.9 (2.8)	21.7 (3.4)
R_{merge} (%)	9.0 (47.5)	5.1 (47.9)
Refinement		
Resolution range (Å)	29.9–3.3 (4.2–3.3)	26.3–2.95 (3.36–2.95)
No. of reflections	6383	9559
No. of reflections (test set)	356	507
R_{work} (%)	20.6 (26.4)	20.4 (26.4)
R_{free} (%)	25.7 (29.9)	23.1 (32.2)
No. atoms; mean atomic displacement parameters (Å^2)		
RNA	2374; 135.6	2394; 98.9
Ligand/ion	40; 143.3	64; 78.8
Water	–	11; 68.9
Deviations from ideal values (rmsd)		
Bonds (Å)	0.002	0.003
Angles (°)	0.517	0.612
ML-based coordinate error (Å)	0.4	0.4
All-atom clashscore, percentile[b]	16.35, 97th	13.00, 96th
PDB ID	2YIF	2YIE

Values for the outer shell are given in parentheses.
[a]Values for the highest resolution shell are given in parentheses.
[b]Calculated by MOLPROBITY (45).

A superimposition of the 3D structures of the free form of *Fnu*M over the FMN-bound form of *Fnu*M and nine structures of *Fnu*O solved previously (19) showed a similar global fold (maximum likelihood rmsd = 0.17 Å; Figure 4a). Structural differences were limited to P1, P4 and J4/5, as inferred previously from the structures of *Fnu*O bound to diverse ligands (19). A comparison between the free and FMN-bound forms of *Fnu*M indicated that with shifts of 3.9 and 4.5 Å between the phosphate atoms of respectively U61 and G62 in the free and FMN-bound structures, the magnitude of the structural changes was the greatest for J4/5. This finding is similar to observations made in several studies of the SAM-I riboswitch aptamer, which found localized flexibility within joining regions and/or the binding pocket provided access for *S*-adenosylmethione to a buried and mostly preorganized binding site (13,48).

Although the backbone atoms of nucleotides in J3/4 are superimposable in the free- and FMN-bound structures, base-stacking alterations occurred upon ligand binding (Figure 4b). In particular, A48 and A49 stack against each other to promote same-strand stacking from P3 through J3/4 to P4 in absence of ligand. But in presence of FMN, A48 stacks instead against the flavin moiety of FMN (19), resulting in a shift of the base of ~3 Å. A49 shifts away from the binding site but remains stacked against P4 (Figure 4b) and forms hydrophobic interactions with FMN (19). Such movements result in the disruption of the Watson–Crick A49–U60 pair, and of the interaction involving the Watson–Crick faces of A48 and U61 (Figure 4c and d; Supplementary Figure S9). Together, these local conformational differences are consistent with the results from the SHAPE surveys (Figures 2 and 3) in that they occur precisely at joining regions J3/4 and J4/5. Furthermore, the higher $[Mg^{2+}]_{1/2}$ values observed for J3/4 in presence of FMN for *F. nucleatum* (Figure 2d) could be accounted for by the reorganization these nucleotides underwent during binding. The fact that no structural differences were observed for joining regions J1/2 and J6/1 could be attributed to the energetic stabilization of similar conformations by crystal packing. But as neighboring molecules are >9 Å away from J1/2 and J6/1, this similarity in conformation could instead suggest these joining regions were able to adopt a pre-folded conformation in absence of ligand.

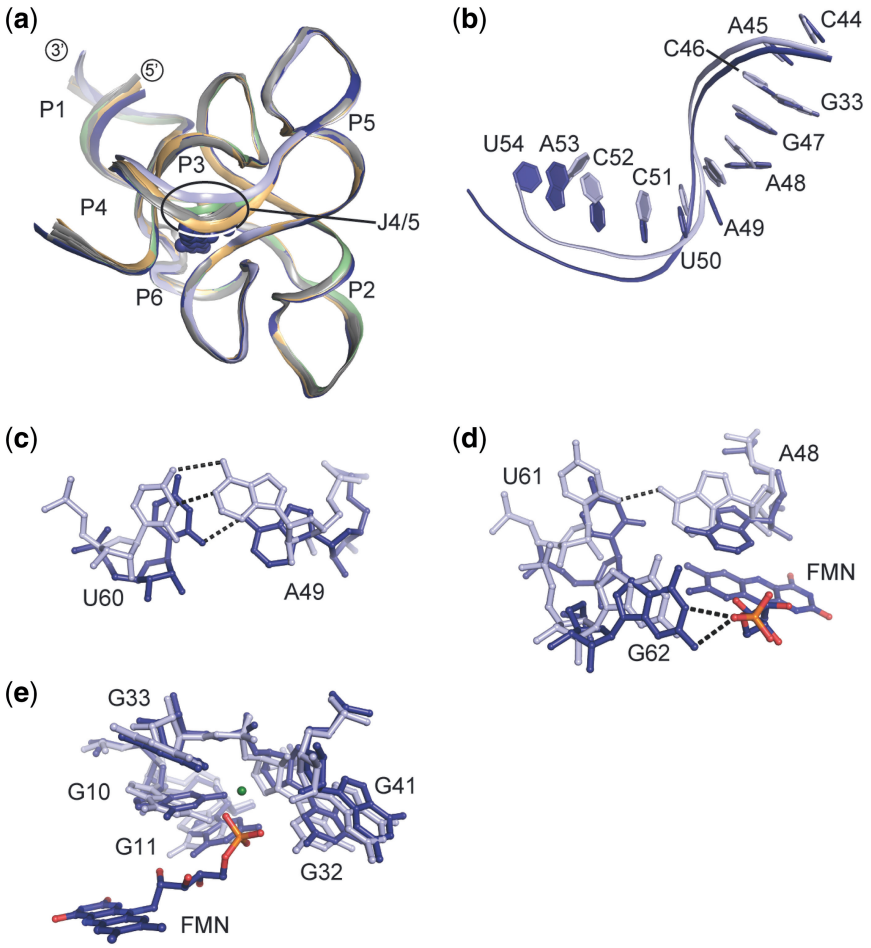

Figure 4. Reorganization of the J3/4 and J4/5 joining regions upon ligand binding. (**a**) Overlay of crystal structures of the *F. nucleatum* riboswitch from this work (light blue, free form, PDB ID 2yif; dark blue, FMN-bound form, PDB ID 2yie) on previously solved structures [gray, five FMN-bound structures; green, FMN-bound structure in presence of cobalt hexamine; gold, Roseoflavin- and Riboflavin-bound structures (19)]. FMN atoms shown as dark blue spheres. (**b**) Base orientations at and near J3/4 in the free and FMN-bound forms. (**c**) and (**d**) Conformational changes at the FMN-binding site. FMN colored per atom type (dark blue carbon atoms). (**e**) A magnesium ion could be present at the binding site only in presence of FMN.

Could the magnesium ion that mediates interactions between FMN and the RNA be absent when FMN is not bound?

As observed for the thiamine pyrophosphate and glycine riboswitches (9,49,50), a cation mediates interactions between the ligand and the RNA in the binding pocket of the FMN riboswitch (19). Specifically, a penta-hydrated magnesium ion is coordinated to N7 of G33 (first coordination sphere) and to oxygen atoms belonging to FMN, G32, U34, G41 and G62 (second coordination sphere) (19). These contacts are also observed in the FMN-bound structure of *Fnu*M (Figure 4d and e). However, no magnesium ion is observed in the free structure at that position (Figure 4e). Additionally, the $[Mg^{2+}]_{1/2}$ values calculated for G33 of *F. nucleatum* are 1.7 ± 0.2 mM in absence of FMN, and 0.3 ± 0.1 mM in presence of FMN (Figure 2d, Supplementary Tables S1 and S2). This ~5-fold decrease of the $[Mg^{2+}]_{1/2}$ value is consistent with a lower occupation of that magnesium-binding site in absence of ligand (further insights could not be gained from the *B. subtilis* equivalent of G33 (residue G57) as it shows no folding cooperativity; Supplementary Figure S3). Nonetheless, two factors could currently account for the absence of a magnesium ion at that site in the free structure: (i) the overall 23% decrease in occupation of magnesium-binding sites (from 14 to 11 sites) between the FMN-bound structure and the free structure of *Fnu*M; (ii) G32, G41, G62 in *F. nucleatum* (and analogously G56, G84, G114 in *B. subtilis*) had the same low $[Mg^{2+}]_{1/2}$ value (<0.5 mM) in both the free and the FMN-bound RNA (Supplementary Tables S1 and S2). As a consequence, while our data suggest that FMN is required to support binding of a magnesium ion at this position, further experiments will be needed to clarify this issue.

DISCUSSION

Prior evidence collected for the FMN aptamer domain pointed at predominantly local conformational changes of the RNA upon FMN binding (17–19). The present

combination of structural studies and chemical probing under conditions that modulate the folding process of the *B. subtilis* and *F. nucleatum* variants of this aptamer allowed us to pinpoint ligand-induced structural changes to four of the six joining regions (J1/2, J3/4, J4/5 and J6/1). Our temperature surveys are consistent between the two RNAs and lead us to propose that J1/2 and J6/1 act as flexible gates to the binding pocket, in a similar fashion to J2/3 in the purine riboswitch (20,32) and to J1/2–J3/4 in the SAM-I riboswitch (13,48). Our findings hint at a distinct but complementary role for J3/4 and J4/5. Both same-strand base stacking interactions involving J3/4 and base pairing interactions between nucleotides in J3/4 and J4/5 keep the binding site in a relatively 'open' state in absence of ligand. These RNA–RNA interactions are replaced by RNA–FMN interactions to support a 'closed' ligand-bound form (Figure 4). The role of J3/4 and J4/5 then seems to be similar to that of A46 in the SAM-I riboswitch (13), in the sense that they prevent a collapse of the binding site, although they do not necessarily act as 'place holders' for the ligand. In short, J1/2 and J6/1 allow access to the binding site, while J3/4 and J4/5 participate in maintaining a structure of the binding pocket that is conducive to ligand binding. Further studies are needed to reveal when and how the uracil-like edge and the ribose-phosphate moiety of FMN are recognized by J1/2, J6/1 and a metal ion (19). Together, such considerations about relative flexibility at the binding site and chronology of binding events would represent crucial knowledge for the most effective drug design strategies that afford to take RNA dynamics into account (51–53).

The globally preorganized and bound-like structure of the free FMN riboswitch aptamer domain is reminiscent of observations of other riboswitches, including the lysine riboswitch (16), the SAM-I, -II and -III riboswitches (13,27–29), the $preQ_1$ riboswitch from *T. tengcongensis* (12), and even an artificial neomycin-dependent riboswitch (54,55). At physiological concentrations of magnesium (typically 0.5–1.5 mM) but in absence of ligand, these riboswitches adopt interconverting conformations, some of which are close in structure to the ligand-bound state. How frequently the closest conformations to the ligand-bound state are sampled by the population of the interconverting free states can be a characteristic of the riboswitch class. For example, TPP riboswitches appear to populate ligand-bound states in absence of ligand far less frequently (17,56) than other classes (11,13,17,32) (Figure 5). Thus, the TPP riboswitches appear to undergo large conformational changes upon ligand binding, whereas lysine and FMN appear to have virtually no ligand-dependent global changes in their architecture.

Even within the same class phylogenetic variants are observed to display different behaviors in their free state. The free states of the SAM-I and $preQ_1$ riboswitches from thermophilic *T. tengcongensis* (12,13) are closer to the bound-like states than their equivalents from mesophilic *B. subtilis* (29) and *F. nucleatum* (12,57) (Figure 5). Together with the guanine riboswitch and the lysine riboswitch from mesophilic *B. subtilis*, the FMN riboswitch from *B. subtilis* and *F. nucleatum* fall in the category of riboswitches whose free states are more frequently closer to the bound-like state.

Regardless of how close to the ligand-bound state the conformational ensemble appears to be, it is very likely that most riboswitches employ *conformational selection* as their mechanism of ligand recognition and productive binding (13,27,28,55,58). Conformational selection occurs when the ligand interacts with the most bound-like population of free states, progressively shifting the binding equilibrium toward the bound state via favorable binding

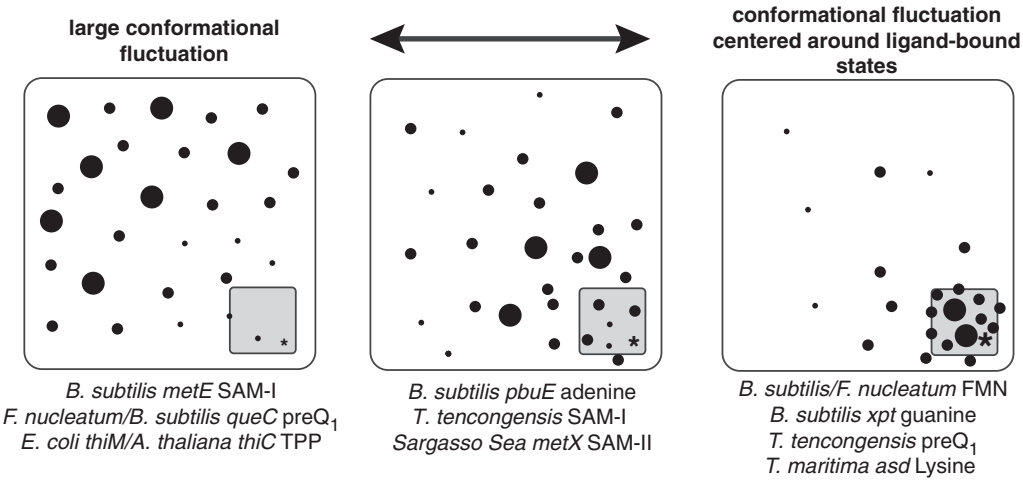

Figure 5. Population dynamics for various riboswitches leading to ligand binding by conformational selection. The large box represents the entire conformational space accessible by the free aptamer RNA. Within this conformational space, individual conformers (e.g. states) are populated to varying degrees at any given point in time. States are represented by dots; the most 'bound-like' state is represented by a star. The larger the symbol, the more populated the state. In this model, an individual RNA rapidly samples different states including those that are unproductive for binding (white region) and those that are 'bound like' and capable of productively interacting with ligand (shaded region). Some riboswitches sparsely sample bound like conformations and thus appear to have large ligand induced conformational changes (left), whereas others more substantially occupy 'bound-like' states, thus appearing to have small ligand induced conformational changes. Representative riboswitches are indicated under each panel (organism, downstream gene, ligand).

energetics (Figure 5) (59). This mechanism had also been observed earlier with other RNA receptors for small molecules like the HIV-transactivation region (60) and the ribosomal-decoding site (61), RNA recognition by ribosomal protein S15 (62), as well as more generally with DNA and protein receptors (59,63,64). Considering that the structures of the population ensemble of free FMN riboswitch aptamer domains are so close to that of the bound state (Figure 5, right), and that a bound-like free state could be crystallized that was able to bind FMN, it is highly likely that ligand binding to the FMN riboswitch similarly happens principally by conformational selection. Subsequent recognition events might include induced fit of J3/4 and J4/5, leading to the compacting of the binding site around FMN seen in the crystal structure of the bound state (Figure 4).

Such ligand-binding events to bound-like conformers that would rapidly shift the ensemble toward populating productive conformers support the kinetic control mechanism that was reported previously for the FMN riboswitch and other riboswitches (5,6,57) and reviewed in (65). Kinetic control is defined by the observation that the concentration of FMN required for half-maximal regulatory response (T_{50}) is greater than its affinity for RNA (K_D). This behavior reflects that the time required for the polymerase to reach the terminator element is shorter than the time required for the aptamer to reach equilibrium with respect to FMN binding (5,6). In the short temporal window the aptamer has to interrogate the cellular environment, minimal ligand-induced structural changes or stabilization make for a more reasonable expectation than major structural reorganizations. In the case of the FMN riboswitch, FMN-induced stabilization of J1/2, J3/4, J4/5 and J6/1 would be sufficient to prevent pairing of the switching sequence at J1/2 with the complementary sequence in the downstream expression platform. Furthermore, how such small changes would lead to the quick genetic decision made by this riboswitch (6) could be illustrated by recent findings using a small self-cleaving RNA (66). Using the hairpin ribozyme as a model system, Mahen *et al*. showed that *in vivo*, fast folding occurs by exchange of base pairs between adjacent RNA secondary structures, and not by complete helix dissociation. Additionally, they discussed how this rapid exchange mechanism could account for the kinetic control of the purine riboswitch. In light of our present findings, such *in vivo* studies with riboswitches should reveal how a small net stabilization of the aptamer domain driven by ligand binding is able to drive the appropriate regulatory response.

ACCESSION NUMBERS

The coordinates and structure factors for the apo- and FMN-bound riboswitch have been deposited in the Protein Data Bank (PDB ID: 2YIF and 2YIE).

SUPPLEMENTARY DATA

Supplementary Data are available at NAR Online.

ACKNOWLEDGEMENTS

The authors would like to thank Annie Héroux for collecting the data as part of the mail-in crystallography program at Brookhaven National Laboratory; Stefanie Mortimer and Kevin Weeks for the gift of 1M7; Francis Reyes and Mickaël Blaise for helpful discussions during data processing and refinement; Alain Laederach for helpful suggestions on the normalization procedure; and Jen Pfingsten, Jeff Kieft, and Ken Blount for comments on the manuscript.

FUNDING

Funding for open access charge: National Institutes of Health (R01 GM083953 to R.T.B.).

Conflict of interest statement: R.T.B. is a paid consultant of BioRelix, a company dedicated to developing antibiotic therapeutics targeted against riboswitches.

REFERENCES

1. Montange,R.K., Mondragon,E., van Tyne,D., Garst,A.D., Ceres,P. and Batey,R.T. (2010) Discrimination between closely related cellular metabolites by the SAM-I riboswitch. *J. Mol. Biol.*, **396**, 761–772.
2. Roth,A. and Breaker,R.R. (2009) The structural and functional diversity of metabolite-binding riboswitches. *Annu. Rev. Biochem.*, **78**, 305–334.
3. Garst,A.D. and Batey,R.T. (2009) A switch in time: detailing the life of a riboswitch. *Biochim. Biophys. Acta*, **1789**, 584–591.
4. Winkler,W.C. and Breaker,R.R. (2003) Genetic control by metabolite-binding riboswitches. *Chembiochem*, **4**, 1024–1032.
5. Wickiser,J.K., Cheah,M.T., Breaker,R.R. and Crothers,D.M. (2005) The kinetics of ligand binding by an adenine-sensing riboswitch. *Biochemistry*, **44**, 13404–13414.
6. Wickiser,J.K., Winkler,W.C., Breaker,R.R. and Crothers,D.M. (2005) The speed of RNA transcription and metabolite binding kinetics operate an FMN riboswitch. *Mol. Cell.*, **18**, 49–60.
7. Batey,R.T., Gilbert,S.D. and Montange,R.K. (2004) Structure of a natural guanine-responsive riboswitch complexed with the metabolite hypoxanthine. *Nature*, **432**, 411–415.
8. Montange,R.K. and Batey,R.T. (2006) Structure of the S-adenosylmethionine riboswitch regulatory mRNA element. *Nature*, **441**, 1172–1175.
9. Thore,S., Leibundgut,M. and Ban,N. (2006) Structure of the eukaryotic thiamine pyrophosphate riboswitch with its regulatory ligand. *Science*, **312**, 1208–1211.
10. Serganov,A. and Patel,D.J. (2007) Ribozymes, riboswitches and beyond: regulation of gene expression without proteins. *Nat. Rev. Genet.*, **8**, 776–790.
11. Garst,A.D., Edwards,A.L. and Batey,R.T. (2010) Riboswitches: structures and mechanisms. *Cold Spring Harb. Perspect. Biol.*, **3**, a003533.
12. Jenkins,J.L., Krucinska,J., McCarty,R.M., Bandarian,V. and Wedekind,J.E. (2011) Comparison of a preQ1 riboswitch aptamer in the metabolite-bound and free states with implications for gene regulation. *J. Biol. Chem.*, doi:10.1074/jbc.M111.230375.
13. Stoddard,C.D., Montange,R.K., Hennelly,S.P., Rambo,R.P., Sanbonmatsu,K.Y. and Batey,R.T. (2010) Free state conformational sampling of the SAM-I riboswitch aptamer domain. *Structure*, **18**, 787–797.
14. Huang,L., Serganov,A. and Patel,D.J. (2010) Structural insights into ligand recognition by a sensing domain of the cooperative glycine riboswitch. *Mol. Cell*, **40**, 774–786.
15. Serganov,A., Huang,L. and Patel,D.J. (2008) Structural insights into amino acid binding and gene control by a lysine riboswitch. *Nature*, **455**, 1263–1267.

16. Garst,A.D., Heroux,A., Rambo,R.P. and Batey,R.T. (2008) Crystal structure of the lysine riboswitch regulatory mRNA element. *J. Biol. Chem.*, **283**, 22347–22351.
17. Baird,N.J. and Ferre-D'Amare,A.R. (2010) Idiosyncratically tuned switching behavior of riboswitch aptamer domains revealed by comparative small-angle X-ray scattering analysis. *RNA*, **16**, 598–609.
18. Winkler,W.C., Cohen-Chalamish,S. and Breaker,R.R. (2002) An mRNA structure that controls gene expression by binding FMN. *Proc. Natl Acad. Sci. USA*, **99**, 15908–15913.
19. Serganov,A., Huang,L. and Patel,D.J. (2009) Coenzyme recognition and gene regulation by a flavin mononucleotide riboswitch. *Nature*, **458**, 233–237.
20. Gilbert,S.D., Stoddard,C.D., Wise,S.J. and Batey,R.T. (2006) Thermodynamic and kinetic characterization of ligand binding to the purine riboswitch aptamer domain. *J. Mol. Biol.*, **359**, 754–768.
21. Noeske,J., Buck,J., Furtig,B., Nasiri,H.R., Schwalbe,H. and Wohnert,J. (2007) Interplay of 'induced fit' and preorganization in the ligand induced folding of the aptamer domain of the guanine binding riboswitch. *Nucleic Acids Res.*, **35**, 572–583.
22. Merino,E., Wilkinson,K., Coughlan,J. and Weeks,K. (2005) RNA structure analysis at single nucleotide resolution by selective 2-hydroxyl acylation and primer extension (SHAPE). *J. Am. Chem. Soc.*, **127**, 4223–4231.
23. Blount,K.F. and Breaker,R.R. (2006) Riboswitches as antibacterial drug targets. *Nat. Biotechnol.*, **24**, 1558–1564.
24. Lee,E.R., Blount,K.F. and Breaker,R.R. (2009) Roseoflavin is a natural antibacterial compound that binds to FMN riboswitches and regulates gene expression. *RNA Biol.*, **6**, 187–194.
25. Barrick,J.E. and Breaker,R.R. (2007) The distributions, mechanisms, and structures of metabolite-binding riboswitches. *Genome Biol.*, **8**, R239.
26. Kazanov,M.D., Vitreschak,A.G. and Gelfand,M.S. (2007) Abundance and functional diversity of riboswitches in microbial communities. *BMC Genomics*, **8**, 347.
27. Wilson,R.C., Smith,A.M., Fuchs,R.T., Kleckner,I.R., Henkin,T.M. and Foster,M.P. (2011) Tuning riboswitch regulation through conformational selection. *J. Mol. Biol.*, **405**, 926–938.
28. Haller,A., Rieder,U., Aigner,M., Blanchard,S.C. and Micura,R. (2011) Conformational capture of the SAM-II riboswitch. *Nat. Chem. Biol.*, **7**, 393–400.
29. Heppell,B., Blouin,S., Dussault,A.M., Mulhbacher,J., Ennifar,E., Penedo,J.C. and Lafontaine,D.A. (2011) Molecular insights into the ligand-controlled organization of the SAM-I riboswitch. *Nat. Chem. Biol.*, **7**, 384–392.
30. Greenleaf,W., Frieda,K., Foster,D., Woodside,M. and Block,S. (2008) Direct observation of hierarchical folding in single riboswitch aptamers. *Science*, **319**, 630–633.
31. Wilkinson,K.A., Merino,E.J. and Weeks,K.M. (2006) Selective 2'-hydroxyl acylation analyzed by primer extension (SHAPE): quantitative RNA structure analysis at single nucleotide resolution. *Nat. Protoc.*, **1**, 1610–1616.
32. Stoddard,C.D., Gilbert,S.D. and Batey,R.T. (2008) Ligand-dependent folding of the three-way junction in the purine riboswitch. *RNA*, **14**, 675–684.
33. Mortimer,S. and Weeks,K. (2007) A fast-acting reagent for accurate analysis of RNA secondary and tertiary structure by SHAPE. *J. Am. Chem. Soc.*, **129**, 4144–4145.
34. Das,R., Laederach,A., Pearlman,S.M., Herschlag,D. and Altman,R.B. (2005) SAFA: semi-automated footprinting analysis software for high-throughput quantification of nucleic acid footprinting experiments. *RNA*, **11**, 344–354.
35. Laederach,A., Das,R., Vicens,Q., Pearlman,S.M., Brenowitz,M., Herschlag,D. and Altman,R.B. (2008) Semiautomated and rapid quantification of nucleic acid footprinting and structure mapping experiments. *Nat. Protoc.*, **3**, 1395–1401.
36. Celander,D. and Cech,T. (1991) Visualizing the higher order folding of a catalytic RNA molecule. *Science*, **251**, 401–407.
37. Wilkinson,K.A., Merino,E.J. and Weeks,K.M. (2005) RNA SHAPE chemistry reveals nonhierarchical interactions dominate equilibrium structural transitions in tRNA(Asp) transcripts. *J. Am. Chem. Soc.*, **127**, 4659–4667.
38. Montange,R.K., Mondragón,E., Tyne,D.v., Garst,A.D., Ceres,P. and Batey,R.T. (2010) Discrimination between closely related cellular metabolites by the SAM-I riboswitch. *J. Mol. Biol.*, **396**, 761–772.
39. Edwards,A.L., Garst,A.D. and Batey,R.T. (2009) Determining structures of RNA aptamers and riboswitches by X-ray crystallography. *Methods Mol. Biol.*, **535**, 135–163.
40. Otwinowski,Z., Minor,W., Carter,C. and Sweet,R. (1997) *Methods in Enzymology*, Vol. 276, Academic Press, New York, pp. 307–326.
41. Emsley,P., Lohkamp,B., Scott,W. and Cowtan,K. (2010) Features and development of Coot. *Acta Crystallogr. D: Biol. Crystallogr.*, **66**, 486–501.
42. Brunger,A.T., Adams,P.D., Clore,G.M., DeLano,W.L., Gros,P., Grosse-Kunstleve,R.W., Jiang,J.S., Kuszewski,J., Nilges,M., Pannu,N.S. *et al.* (1998) Crystallography & NMR system: A new software suite for macromolecular structure determination. *Acta Crystallogr. D Biol. Crystallogr.*, **54**, 905–921.
43. Adams,P.D., Afonine,P.V., Bunkoczi,G., Chen,V.B., Davis,I.W., Echols,N., Headd,J.J., Hung,L.W., Kapral,G.J., Grosse-Kunstleve,R.W. *et al.* (2010) PHENIX: a comprehensive Python-based system for macromolecular structure solution. *Acta Crystallogr. D Biol. Crystallogr.*, **66**, 213–221.
44. Afonine,P.V., Urzhumtsev,A., Grosse-Kuntsleve,R.W. and Adams,P.A. (2010) Atomic Displacement Parameters (ADPs), their parameterization and refinement in PHENIX. *Computational Crystallogr. Newslett.*, **1**, 24–31.
45. Chen,V.B., Arendall,W.B. 3rd, Headd,J.J., Keedy,D.A., Immormino,R.M., Kapral,G.J., Murray,L.W., Richardson,J.S. and Richardson,D.C. (2010) MolProbity: all-atom structure validation for macromolecular crystallography. *Acta Crystallogr. D Biol. Crystallogr.*, **66**, 12–21.
46. Theobald,D.L. (2006) THESEUS: maximum likelihood superpositioning and analysis of macromolecular structures. *Bioinformatics*, **22**, 2171–2172.
47. Vicens,Q., Gooding,A.R., Laederach,A. and Cech,T.R. (2007) Local RNA structural changes induced by crystallization are revealed by SHAPE. *RNA*, **13**, 536–548.
48. Lu,C., Ding,F., Chowdhury,A., Pradhan,V., Tomsic,J., Holmes,W.M., Henkin,T.M. and Ke,A. (2010) SAM recognition and conformational switching mechanism in the Bacillus subtilis yitJ S box/SAM-I riboswitch. *J. Mol. Biol.*, **404**, 803–818.
49. Huang,L., Serganov,A. and Patel,D.J. (2010) Structural insights into ligand recognition by a sensing domain of the cooperative glycine riboswitch. *Mol. Cell.*, **40**, 774–786.
50. Serganov,A., Polonskaia,A., Phan,A.T., Breaker,R.R. and Patel,D.J. (2006) Structural basis for gene regulation by a thiamine pyrophosphate-sensing riboswitch. *Nature*, **441**, 1167–1171.
51. Moitessier,N., Therrien,E. and Hanessian,S. (2006) A method for induced-fit docking, scoring, and ranking of flexible ligands. Application to peptidic and pseudopeptidic beta-secretase (BACE 1) inhibitors. *J. Med. Chem.*, **49**, 5885–5894.
52. Lang,P.T., Brozell,S.R., Mukherjee,S., Pettersen,E.F., Meng,E.C., Thomas,V., Rizzo,R.C., Case,D.A., James,T.L. and Kuntz,I.D. (2009) DOCK 6: combining techniques to model RNA-small molecule complexes. *RNA*, **15**, 1219–1230.
53. Vicens,Q. (2009) RNA's coming of age as a drug target. *J. Incl. Phenom. Macro.*, **65**, 171–188.
54. Weigand,J.E., Schmidtke,S.R., Will,T.J., Duchardt-Ferner,E., Hammann,C., Wohnert,J. and Suess,B. (2010) Mechanistic insights into an engineered riboswitch: a switching element which confers riboswitch activity. *Nucleic Acids Res.*, **39**, 3363–3372.
55. Duchardt-Ferner,E., Weigand,J.E., Ohlenschlager,O., Schmidtke,S.R., Suess,B. and Wohnert,J. (2010) Highly modular structure and ligand binding by conformational capture in a minimalistic riboswitch. *Angew. Chem. Int. Ed. Engl.*, **49**, 6216–6219.
56. Ali,M., Lipfert,J., Seifert,S., Herschlag,D. and Doniach,S. (2010) The ligand-free state of the TPP riboswitch: a partially folded RNA structure. *J. Mol. Biol.*, **396**, 153–165.

57. Rieder,U., Kreutz,C. and Micura,R. (2010) Folding of a transcriptionally acting preQ1 riboswitch. *Proc. Natl Acad. Sci. USA*, **107**, 10804–10809.
58. Hammond,M.C. (2011) RNA folding: A tale of two riboswitches. *Nat. Chem. Biol.*, **7**, 342–343.
59. Boehr,D.D. and Wright,P.E. (2008) Biochemistry. How do proteins interact?. *Science*, **320**, 1429–1430.
60. Zhang,Q., Sun,X., Watt,E.D. and Al-Hashimi,H.M. (2006) Resolving the motional modes that code for RNA adaptation. *Science*, **311**, 653–656.
61. Vaiana,A.C. and Sanbonmatsu,K.Y. (2009) Stochastic gating and drug-ribosome Interactions. *J. Mol. Biol.*, **386**, 648–661.
62. Batey,R.T. and Williamson,J.R. (1998) Effects of polyvalent cations on the folding of an rRNA three-way junction and binding of ribosomal protein S15. *RNA*, **4**, 984–997.
63. Lange,O.F., Lakomek,N.A., Fares,C., Schroder,G.F., Walter,K.F., Becker,S., Meiler,J., Grubmuller,H., Griesinger,C. and de Groot,B.L. (2008) Recognition dynamics up to microseconds revealed from an RDC-derived ubiquitin ensemble in solution. *Science*, **320**, 1471–1475.
64. Boehr,D.D., Nussinov,R. and Wright,P.E. (2009) The role of dynamic conformational ensembles in biomolecular recognition. *Nat. Chem. Biol.*, **5**, 789–796.
65. Zhang,J., Lau,M.W. and Ferre-D'Amare,A.R. (2010) Ribozymes and riboswitches: modulation of RNA function by small molecules. *Biochemistry*, **49**, 9123–9131.
66. Mahen,E.M., Watson,P.Y., Cottrell,J.W. and Fedor,M.J. (2010) mRNA secondary structures fold sequentially but exchange rapidly in vivo. *PLoS Biol.*, **8**, e1000307.
67. Leontis,N. and Westhof,E. (2001) Geometric nomenclature and classification of RNA base pairs. *RNA*, **7**, 499–512.